

Nanoparticle Patterning on 128-YX-LN Substrates: The Effects of Surface Acceleration and Boundary Layer Streaming

Ming K. Tan, James R. Friend and Leslie Y. Yeo
 Micro/Nanophysics Research Laboratory
 Monash University, Clayton,
 VIC 3800, Australia.
 Email: james.friend@eng.monash.edu.au

Abstract—Nanoparticle patterning on a vibrating solid surface according to the vibration modes of the solid is the result of extremely high solid surface acceleration and persistent flow beyond the steady boundary layer. The solid surface acceleration magnitude increased proportionally to the square of vibration angular frequency. The tens-of-megahertz frequency cause the surface acceleration to reach to an order of 10^7 m/s², and thus providing a substantial impact force when a nanoparticle fall on the solid surface. On the other hand, the acoustic radiation pressure and acoustic streaming drag due to the persistent flow beyond the steady boundary layer transport lifted nanoparticles to an adjacent region where the adhesion force overcomes the impact force.

I. INTRODUCTION

When powder particles are deposited onto a vibrating plate, the various modes at which the plate is excited becomes apparent by observing the formation of unique particle patterns on the plate surface. These so-called *Chladni figures* [1], obtained under low frequency ($f \ll 10^6$ Hz) surface excitation, appear as coarse particles are seen to eject from antinodal regions and settle onto the nodal regions of the vibrating surface [1] whereas finer particles, in contrast, are observed to bounce off the nodal regions and collect on the antinodal regions [2]. More recently, experiments have shown using micro-cantilevers [3] and surface acoustic waves (SAWs) [4] that similar micro/nanoparticle patterns appear on the surfaces of the devices which are typically excited at $f > 10^6$ Hz, significantly higher than those encountered in the classical experiments of Chladni and Faraday described above. For nanoparticle patterning, we differentiate between coarse and fine particles according to their diameter ϕ_p relative to the thickness of the viscous boundary layer, $\delta_v = \sqrt{(2\mu)/(\rho\omega)}$, in which μ and ρ are the fluid viscosity and density, respectively: coarse particles are those with diameters $\phi_p > \delta_v$ and fine particles are those with diameters $\phi_p < \delta_v$.

The first experiments in which particle formation were generated by SAW in an ambient environment was first reported by Reeder *et al.* [5] on lithium niobate, and later by Kolomenskii *et al.* [6] on silicon substrates. Noting the limitation that the particle size employed should be significantly smaller than the acoustic wavelength in the solid

in order to achieve sufficient image resolution, submicron to nanometer particles were employed in these studies. The results of Reeder *et al.* [5] and Kolomenskii *et al.* [6] seem to agree with the original observations of Chladni and Faraday at low frequencies wherein the coarse particles were observed to be shaken or bounced off the high vibration amplitude (antinodal) regions and settled at the nodal positions. In an alternative method using airborne nanoparticles which are one order of magnitude smaller than that used by Reeder *et al.*, the SAW device was used to demonstrate the patterning of these nanoparticles without special handling of the nanoparticles [4].

The SAW constitutes a Rayleigh wave that is generated on the 128-YX-LN substrate and propagates at a velocity $v_{SAW} \approx 3990$ m/s. When the 128-YX-LN is in contact with a fluid medium in which sound propagates slower than v_{SAW} ($c_0 \approx 1450$ m/s for water), *leaky* SAW is generated. The *leaky* SAW radiates substantial amounts of energy from the solid into the fluid. The radiated wave propagates in the fluid medium at the Rayleigh angle $\theta_{SAW} = \sin^{-1}(c_0/v_{SAW})$, giving rise to a pressure front that is sufficient to result in a strong body force on the fluid such that the fluid is driven along the Rayleigh angle [7]. However, when *Leaky*-SAW propagates in air, almost no bulk fluid motion is induced along the direction of Rayleigh angle. This is related to the difference in acoustic impedance between the two media [8]. Assuming the acoustic pressure p_1 and the fluid particle velocity u_1 are in phase, the real part of the acoustic impedance can be defined as $Z = \rho_0 c_\phi$ (kgm⁻²s⁻¹), where c_ϕ is the phase speed of the compressional wave. The approximate orders of magnitude of acoustic impedance for sound traveling in air, water, and 128-YX-LN are $Z_a \approx 10^3$, $Z_w \approx 10^6$, and $Z_{LN} \approx 10^7$. Considering only the normally incident sound waves between the solid-fluid interface, the reflection coefficient is $R = (Z_2 - Z_1)/(Z_2 + Z_1)$ and the percentage of acoustic energy transmitted from the solid into the fluid is $\approx (1 - |R|^2) \times 100\%$. Using this approximation, the amount of acoustic energy transmitted into the fluid when 128-YX-LN is coupled with air versus water is $\approx 2\%$ and $\approx 33\%$, respectively. This tiny amount of transmitted energy into the air has a profound effect on the viscous boundary

layer (δ_v) where fluid viscous and thermal dissipations are at a maximum. In the ambient gas environment, the viscous boundary layer thicknesses $\delta_v \approx 4.9 \times 10^{-7}$ m at 20 MHz frequency. The dissipated acoustic energy in this thin layer of fluid essentially imposes a nonlinear effect that drives fluid to flow transversely on top of the substrate.

II. EXPERIMENTAL METHOD AND RESULTS

For our experiments, we fabricate a collection of 20 MHz, 30 MHz, 50 MHz and 130 MHz bi-directional straight-electrode interdigital transducer (IDT) on 128-YX-LN. We also fabricate curved-electrode transducer that allow focussing of the SAW, thus providing a means for increasing the intensity of the SAW [9], [10], [11]. Without an absorbing gel on the edges of the substrate, a strong standing SAW is generated on the substrate when high excitation power was applied to the bi-directional IDT, thus providing a convenient mechanism for determining the exact location of the patterns formed by the deposited particles, whether at the nodal or antinodal positions. The focusing transducers, on the other hand, were used to analyze the mechanism when the SAW consists of a propagating wave.

A transparent glass chamber 25 mm in height, 23 mm in width and 75 mm in length provides sufficient space for streaming to develop into steady state was constructed. Smoke particles were released into the chamber using a straw. Fresh smoke particles have typical sizes ranging from 40 nm to 500 nm, with a mean diameter of $0.17 \mu\text{m}$ [12], [13]. To determine their actual distributions, we employ a Scanning Mobility Particle Sizer (TSI 3936, Shoreview, MN, USA). The measured particle size distribution is between 60 nm and 1000 nm with a mean of 250 nm.

A micro-lens (AF Micro 60 mm f/2.8D, Nikon, Japan) was mounted on to a high definition video camera (DC300, XL Imaging Ltd., UK) to record the flow field at 7.5 frames per second. After operating the SAW device at high input power within the confinement of the glass chamber, the devices were examined under a microscope (Olympus BXFM, Olympus, Australia) with $2\times$, $10\times$ and $20\times$ magnification lenses. The smoke particle patterns are then compared with surface displacement magnitudes obtained for the same devices using a Laser Doppler Vibrometer (LDV, MSA-400, Polytec PI, Waldbrunn, Germany).

Figures 1–2 show the deposited smoke particles on the surface of the SAW devices. Figures 1(a) and 1(b), in particular, exhibit the distinct parallel lines on the surface of the substrate of the bi-directional 20 MHz device after 30 s of exposure to the smoke; recall that since no absorbing gels were employed to prevent wave reflection, the vibration generated by the bi-directional transducers consists of a standing SAW. The surface vibrations characterised by the LDV, on the other hand, is shown in Fig. 1(c). A comparison between these figures reveal that the dark streaks corresponding to the highly concentrated particle deposition regions in Fig. 1(b) coincide with the nodal lines where the vibration amplitudes are minimal. The surface acoustic wave launched on the 128-YX-LN

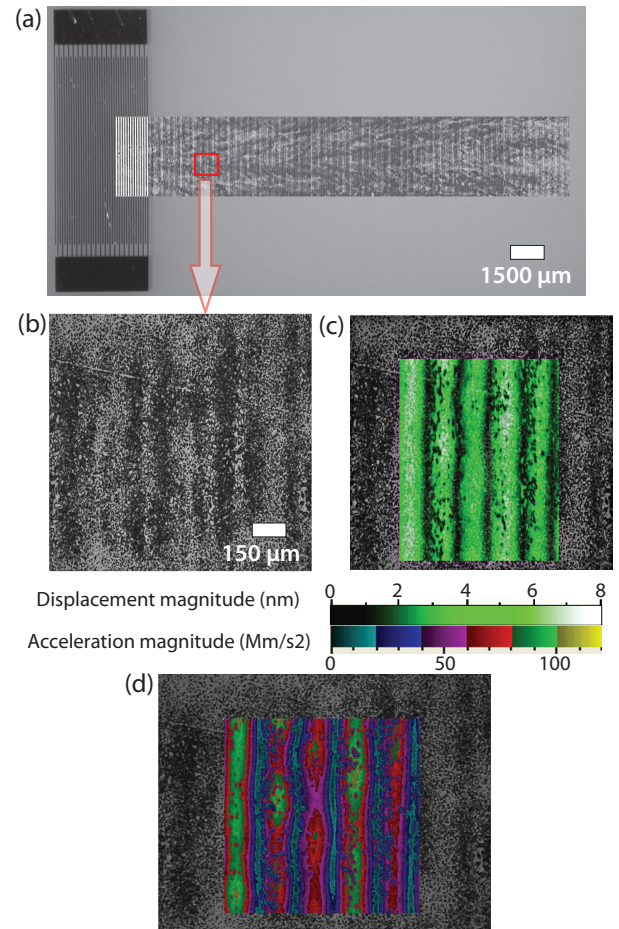


Fig. 1. (a) Photographic images obtained by optical microscopy showing the patterns formed by the deposited smoke particles onto the substrate containing the 20 MHz bi-directional IDT after 30 s delivery of smoke to the glass chamber. The dark streaks indicate the regions of high particle concentration. Due to wave reflection from the edges of the substrate at the excitation voltage of 10^2 mV_{p-p}, a standing wave is formed on the surface of the substrate with a vibration magnitude below 10nm. (b) 10X magnification of the image in (a). (c) and (d) Overlay of the scans obtained from the LDV measurement of the surface acceleration magnitude for the same device, clearly showing the deposition of the smoke particles onto nodal lines.

substrate has an extremely high acceleration magnitude, on the order of $\mathcal{O}(10^8)$ m/s² [Fig. 1 (d)]. However, whilst the surface acceleration magnitude is in the 10^8 m/s² range, the surface displacement magnitude is less than 10 nm [Fig. 1 (c)].

Further confirmation that the smoke particles are being deposited at positions adjacent to the high vibration magnitude regions, e.g., the nodes for standing-SAW, is obtained from the results for the 30 MHz elliptical focusing transducer. Due to the focusing effect, a propagating SAW is generated as the waves do not reflect perpendicularly off the substrate edges and hence do not directly superimpose to form pure standing waves. After 15 s of exposure to the smoke, particle deposition patterns such as that shown in Fig. 2 are observed. Similar deposition patterns are also observed for the 50 MHz and 135 MHz elliptical transducers with the same eccentricity, as

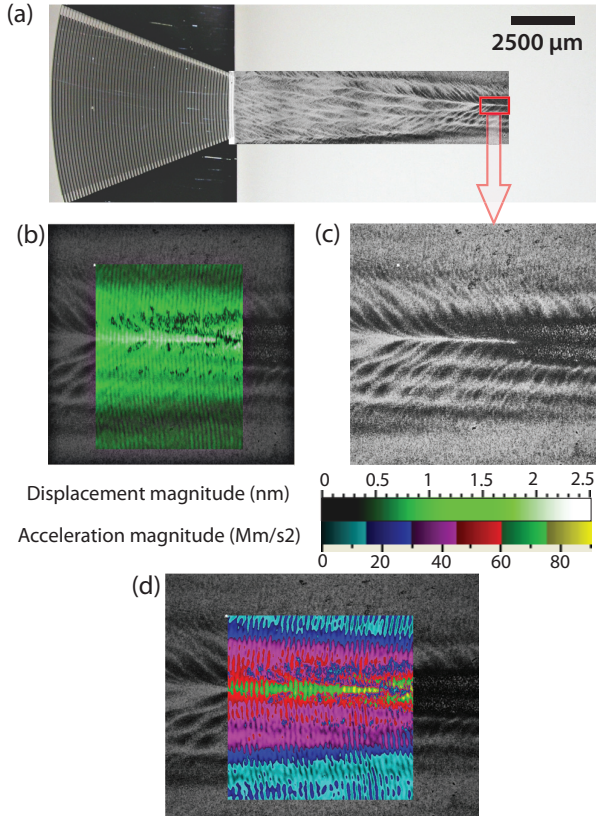


Fig. 2. (a) Photographic images obtained by optical microscopy showing the patterns formed by the smoke particles that deposit onto the surface of the substrate on which a 30 MHz focusing elliptical transducer with 0.616 eccentricity is fabricated after 15 s of smoke delivery to the glass chamber. The dark streaks indicate the regions of high particle concentration. (b) Overlay of the displacement magnitude of the surface wave measured using LDV onto the photographic image of the particle deposition patterns in (a) indicating that the smoke particles are deposited at regions adjacent to the high vibration magnitude. (d) Magnification of the focussed SAW region showing the pattern of the particle deposition there, and, (e) similar overlay of the LDV surface displacement and acceleration, again showing good agreement with the observed particle deposition patterns.

shown in Fig. 3. Figure 2(b) shows the vibration displacement magnitude measured using LDV, indicating that the smoke particles deposit onto the regions immediately adjacent to high vibration displacement magnitude regions.

The particle deposition onto the vibrating substrate is enhanced by acoustic streaming that is generated by the SAW within the the glass compartment. Figure 4 shows an experimental image of the induced air flow due to acoustic streaming; the direction of the air flow is indicated by the arrows and appears to be in the opposite direction to that of the SAW propagation. This image was captured at the front section of the transparent chamber where the SAW device is located. Once the electrical signal is applied, the air flow due to the acoustic streaming becomes visible under a minute. The chamber walls interrupt the steady flow of air in the direction opposite to the direction of SAW propagation, and the air stream is squeezed through the small gap between

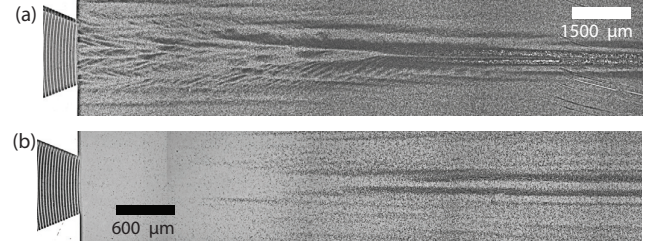


Fig. 3. Particle deposition patterns after 15 s of exposure on the surface of the (a) 50 MHz (a), and, (b) 135 MHz focussing elliptical transducers of 0.616 eccentricity.

the chamber wall and the SAW device. This unstable flow region prevents smoke particles from escaping the chamber and redirects the steady air stream upwards, giving rise to a recirculatory flow above the device. This recirculating air flow in the bulk fluid region convects the suspended smoke particles into the boundary layer immediately adjacent to the surface of the device, thereby enhancing the deposition of the particles onto the surface.

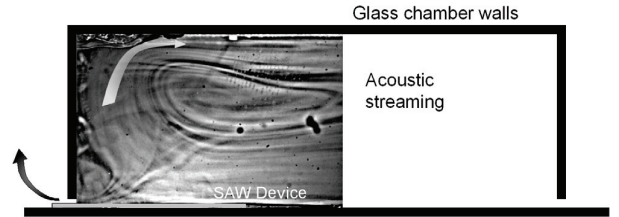


Fig. 4. Experimental image showing the air flow (acoustic streaming) above the SAW device within the confines of the enclosed glass chamber. The flow direction is counter-clockwise—just above the substrate, the air flow is therefore in the opposite direction to that of the SAW propagation.

III. NUMERICAL MODEL AND RESULTS

A simple two-dimensional numerical model was constructed to estimate the magnitude of the acoustic pressure acting on the nanoparticles and to show that the air flow (see Fig. 4) is due to the boundary layer streaming. The calculated acoustic pressure and streaming velocities are then used in the next Section to estimate the magnitude of primary forces and subsequently to explain the primary mechanism that gives rise to the particle deposition patterns observed in Section II. The equation of motion that describes the velocity components v_j in the solid substrate are $\rho_s(\partial v_j / \partial t) = \partial T_{ij} / \partial x_i$, where ρ_s is the density of the piezoelectric crystal, t the time and T_{ij} the stress tensor. These are complimented by the piezoelectric constitutive relationships, which when formulated in the time-domain, read [14], [15], [16],

$$\frac{\partial D_i}{\partial t} = e_{ikl} \frac{\partial S_{kl}}{\partial t} + \epsilon_{ik}^S \frac{\partial E_k}{\partial t}, \quad (1)$$

$$\text{and} \quad \frac{\partial T_{ij}}{\partial t} = c_{ijkl}^E \frac{\partial S_{kl}}{\partial t} - e_{kij} \frac{\partial E_k}{\partial t}, \quad (2)$$

where D_i is the electric displacement vector, e_{ikl} the piezoelectric constant, S_{kl} the mechanical strain, ϵ_{ik}^S the dielectric constant, E_k the electric field, and, c_{ijkl}^E the elastic stiffness constant, respectively. Quasi-static approximation is assumed such that the electromagnetic wave propagation in Eq. (1) can be neglected, i.e., $\partial \mathbf{D} / \partial t \approx 0$. Closure to the above set of equations is then obtained through the relationship between the strain and particle displacement [14], $S_{kl} = 1/2 (\partial \xi_k / \partial x_l + \partial \xi_l / \partial x_k)$, where ξ_k is the displacement of the particle elements constituting the solid.

In the fluid phase, a regular perturbation expansion of the fluid velocity, pressure, density and temperature fields in the asymptotically small $\varepsilon = U/c_0$ limit, wherein U is the characteristic scale of the local velocity of the fluid elements and c_0 is the speed of sound, is applied to the equations governing the conservation of mass, energy and momentum [17], [18], [19], [20]. Two thermodynamic relations are used to complete the set of equations $d\rho_f = (\gamma/c^2)dp - \alpha\rho_f dT$ and $ds = c_p(dT/T) - (\alpha/\rho_f)dp$, where c is the sound speed, α the volumetric thermal expansion coefficient, and, $\gamma = c_p/c_v$ is the adiabatic index, in which c_p and c_v are the specific heat capacities of the fluid at constant pressure and constant volume, respectively. Expansion of the governing fluid equations and the corresponding thermodynamic relationships then result in the following $\mathcal{O}(\varepsilon)$ first order approximations [18], [19], [20]:

$$\rho_{f0} \frac{\partial \mathbf{u}_1}{\partial t} = -\nabla p_1 + \mu \nabla^2 \mathbf{u}_1 + \left(\mu_B + \frac{\mu}{3} \right) \nabla \nabla \cdot \mathbf{u}_1, \quad (3)$$

$$\frac{\partial p_1}{\partial t} = \frac{c_0^2 \rho_{f0}}{\gamma_0} \left(\alpha_0 \frac{\partial T_1}{\partial t} - \nabla \cdot \mathbf{u}_1 \right), \quad (4)$$

$$\text{and} \quad \frac{\rho_{f0} c_{p0}}{\kappa_0} \frac{\partial T_1}{\partial t} = \frac{\alpha_0 T_0}{\kappa_0} \frac{\partial p_1}{\partial t} + \nabla^2 T_1. \quad (5)$$

In the above, ρ_f is the fluid density, \mathbf{u} the fluid velocity, p the pressure, μ the shear viscosity, μ_B the bulk (or dilatational) viscosity, T the temperature and κ the thermal conductivity. The zeroth terms denoted by the subscript '0' refers to the unperturbed equilibrium state. The first order approximations are denoted by the subscript '1' and provide the solution of the propagation of the sound wave in the fluid. The time-averaged second-order approximation can be written as [18], [19], [21]

$$\mathbf{F}_{dc} = - \left\langle \rho_{f1} \frac{\partial \mathbf{u}_1}{\partial t} \right\rangle - \rho_{f0} \langle (\mathbf{u}_1 \cdot \nabla) \mathbf{u}_1 \rangle, \quad (6)$$

$$\text{and} \quad \mathbf{F}_{dc} = \rho_{f0} \frac{\partial \mathbf{u}_{dc}}{\partial t} + \nabla p_{dc} - \mu \nabla^2 \mathbf{u}_{dc}. \quad (7)$$

where the parentheses $\langle \rangle$ denote time-averaging of the inner quantity. \mathbf{F}_{dc} is the body force density (N/m^2) that arising from the forcing of the first order acoustic field, p_{dc} is the second order pressure, and, \mathbf{u}_{dc} is the second order streaming velocity.

Figure 5(a) show the transmitted sound velocity field in air after 6 cycles of the applied sinusoidal electrical signal. The velocity vector plot for the acoustic streaming is also shown in Fig. 5(b). Close observation at Fig. 5(b), reveals that the direction of the air flow that is generated is opposite to

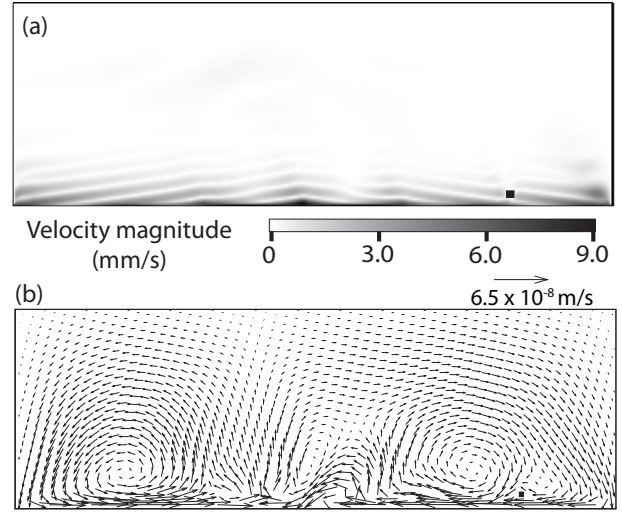


Fig. 5. Contour plot (a) of the first order sound velocity field and vector plot (b) of the second order fluid velocity. The location of a fluid element that we pick to track the velocities is represented by the black square in the figure.

the direction of the SAW propagation, which is in qualitative agreement with the experimental results observed in which the recirculating air flow rotates in a clockwise direction above the forward propagating wave. In addition, we also observe from Fig. 5(b) that the flow is predominantly restricted to the thin viscous boundary layer.

IV. PARTICLE SURFACE PATTERNING

Having numerically determined the acoustic pressure from the first order sound field and acoustic streaming velocity from the second order approximation acting on the particle, we now turn our attention to examine plausible mechanisms by which the patterning of fine particles on the SAW substrate occurs. In general, both particle-solid and particle-fluid interactions need to be considered. The particle-solid interactions for a particle in contact with the solid surface consist of adhesive (van der Waals and capillary) forces as well as repulsive (electrostatic and electric double layer) forces [22]. Particle-fluid interactions arise due to the drag and lift/buoyancy forces that act on the particle due to the steady streaming of the fluid around the particle. In addition, the impact force exerted by the surface on the particle during contact due to the large acceleration encountered when the surface is excited by the SAW at MHz order frequencies also has to be taken into account. Other surface and body forces acting on the particle include the acoustic radiation pressure and gravitational forces. In what is to follow, we will consider an order of magnitude analysis of the forces acting on the particle in order to determine the dominant forces acting on the particle and hence elucidate the driving mechanisms that are responsible for the patterning of the particles on the vibrating surface.

For air-loading, there are no double layer interactions. Moreover, assuming that there are no excess charges on the solid or particle surfaces that give rise to electrostatic interactions and

that the humidity is insignificant such that condensation of water vapour onto the surface to form a meniscus between the particle and solid surfaces can be neglected, the only particle-solid interaction that we will take into account is the van der Waals force. Thus, for a particle on a solid substrate exposed to air, the forces acting on the particle are: (1) the van der Waals force, (2) the gravitational force, (3) the impact force, (4) the acoustic radiation force, and, (5) the drag force. Assuming the particle to be a deformable sphere, the van der Waals force is [23], $F_{\text{vdW}} = (AR_p)/(6z^2)$, where A is the Hamaker constant, R_p is the particle radius, z is the adhesional distance and a is the contact radius between the deformed particle and the solid surface. Assuming $A \approx 10^{-19}$ J in atmospheric conditions, $z \approx 10^{-10}$ m and $R_p \approx 10^{-9}$ nm, $F_{\text{vdW}} \sim \mathcal{O}(10^{-8})$ N.

Assuming a smoke particle has mean particle mass $m_p \approx 10^{-9}$ g, the gravitational force, $F_{\text{gv}} = m_p g$, where g is the gravitational acceleration, is roughly on the order (10^{-10}) N. The impact force acting on the particle when it bounces and hence collides with the vibrating surface, on the other hand, can be determined from $F_{\text{Imp}} = m_p a_s$, where a_s is the acceleration of the piezoelectric substrate. Generally, vibration generated on a piezoelectric substrate imparts a velocity of 1 m/s on an element on the substrate surface, independent of the frequency. Given the typical displacement of the element is around 10 nm, the surface acceleration is roughly 10^7 m/s²; this is corroborated by the experimental measurements using the LDV, as shown by Figs. 1 and 2. The therefore particle experiences an impact force on the order of (10^{-4}) N.

To estimate the acoustic radiation pressure, we determine the pressure distribution on the surface of a particle through our numerical simulation. The x_1 - and x_3 -components of the acoustic radiation pressure forces is then calculated from $F_{\text{Rad}}^x = -(\partial p_1/\partial x)V_p$ and $F_{\text{Rad}}^y = -(\partial p_1/\partial y)V_p$, respectively, where V_p is the volume of the particle. Using the numerical results, the magnitude of the acoustic radiation pressure force are approximately $F_{\text{Rad}}^x \approx -10^{-15}$ N and $F_{\text{Rad}}^y \approx 10^{-15}$ N. Finally, the drag/lift force acting on the particle due to the acoustic streaming generated in the fluid due

TABLE I
ORDER OF MAGNITUDE ESTIMATES FOR THE VARIOUS FORCES ACTING ON A PARTICLE ON THE SURFACE ALONG WHICH THE SAW PROPAGATES FOR DIFFERENT PARTICLE RADII R_p .

Force	$R_p \sim 10^{-7}$ m	$R_p \sim 10^{-8}$ m	$R_p \sim 10^{-9}$ m
$F_{\text{vdW}} \propto R_p$	10^{-8} N	10^{-9} N	10^{-10} N
$F_{\text{gv}} \propto R_p^3$	10^{-10} N	10^{-13} N	10^{-16} N
$F_{\text{Imp}} \propto R_p^3$	10^{-4} N	10^{-7} N	10^{-10} N
$F_{\text{Rad}} \propto R_p^2$	10^{-15} N	10^{-17} N	10^{-19} N
$F_{\text{lift}}^{dc} \propto R_p$	10^{-16} N	10^{-17} N	10^{-18} N
F_p^y	$+10^{-4}$ N	$+10^{-7}$ N	-10^{-16} N
F_p^x	-10^{-15} N	-10^{-17} N	-10^{-19} N

to the SAW can be approximated from $F_{\text{drag/lift}}^{dc} = \mu R_p u_{dc}$. Based on the estimated streaming velocities, the streaming drag along the x_1 - and x_3 -directions are $F_{\text{lift}}^{dc(x)} \sim (10^{-16})$ N and $F_{\text{drag}}^{dc(y)} \sim (10^{-17})$ N, respectively.

The forces acting on the particle and their relative order of magnitudes are summarised in Fig. 6. Initially, smoke particles deposit randomly on the surface of the substrate in the absence of the SAW. Upon applying the oscillating electrical signal and hence the generation and propagation of the SAW across the substrate, the particles that have deposited randomly on the surface acquire the possibility to be ejected from the large displacement amplitude regions. For this removal process to be possible, the particles have to be ejected off the surface and subsequently transported to a new location. Particle ejection, however, can only take place if the particle suffers from a net vertical force in the upward direction. Two lift mechanisms are postulated. One possibility is the impact force imparted by the surface on the particles due to the extremely large surface acceleration. The other is the lift force generated on the particle either due to the acoustic radiation pressure or the acoustic streaming of the fluid surrounding the particle. On the other hand, the lift is retarded by the gravitational force and by van der Waals forces if the particle is in contact with the substrate. The net vertical force exerted on the particle is therefore, $F_p^y = F_{\text{Imp}} + F_{\text{Rad}}^y - F_{\text{gv}} - F_{\text{lift}}^{dc(y)} - F_{\text{vdW}}$.

Once the particles are ejected from the high displacement amplitude regions on the surface, the transverse acoustic radiation pressure and acoustic streaming drag force transport the dislodged particles to the adjacent low amplitude regions, where gravitational and adhesion forces are sufficient to overcome the impact force at these low acceleration regions. We note that both the transverse acoustic radiation pressure and drag force are in the same direction, opposite to the direction of SAW propagation. A force-balance in the transverse direction then yields $F_p^x = -F_{\text{Rad}}^x - F_{\text{drag}}^{dc(x)}$.

The order of magnitude estimates of the various forces acting on the particle as well as the net vertical and horizontal

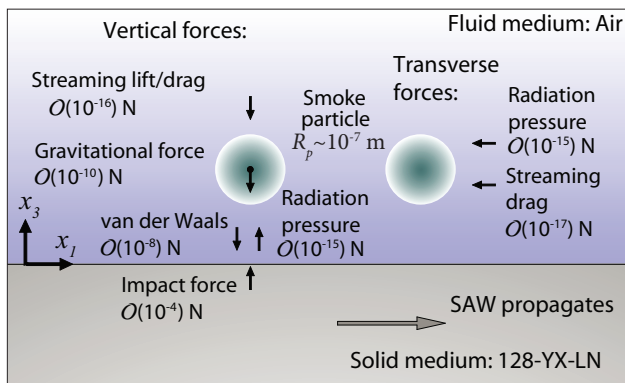


Fig. 6. Schematic illustration of the forces acting on a particle on the surface along which a SAW propagates.

forces on the particle are tabulated in Table I for particles of different radii R_p . We observe therefore that the net vertical force is positive, i.e., there is an upward force on the particle such that it is lifted off the surface, for $R_p > 10^{-8}$ m. Clearly, the impact force, which is the dominant mechanism by which particles are ejected off the surface and scales as the cubic power of R_p , decays very quickly as the particle size decreases, leading to a reduction in the ejection probability for very small particle sizes below 10 nm.

V. CONCLUSIONS

The major results presented here are: (1) airborne smoke particles ($\phi_p \approx 300$ nm) are distributed in regions where acceleration magnitude is low (see Fig. 1 and Fig. 2), (2) steady air streaming is observed and the direction is opposite to the direction of SAW propagation, (3) impact force is greatly dominant and responsible for bouncing the nanoparticles off the highly accelerating regions (see Table I), and, (4) acoustic radiation pressure and acoustic streaming transport lifted particles transversely and to regions where adhesion forces overcome impact force (see Table I). To assist in the analysis of the magnitude orders of all the major forces, in particularly the nonlinear forces, we have constructed a simple numerical model. Numerical results for the acoustic streaming quantitatively agree with the experimental result that air flows in the direction opposite to SAW propagation and is driven by the boundary layer streaming.

REFERENCES

- [1] E. Chladni, *Entdeckungen über die Theorie des Klanges*. Weidmanns, Erben und Reich, 1787.
- [2] M. Faraday, "On a Peculiar Class of Acoustical Figures; and on Certain Forms Assumed by Groups of Particles upon Vibrating Elastic Surfaces," *Philosophical Transactions of the Royal Society of London*, vol. 121, pp. 299–340, 1831.
- [3] M. Dorrestijn, A. Bietsch, T. Açıkalın, A. Raman, M. Hegner, E. Meyer, and C. Gerber, "Chladni Figures Revisited Based on Nanomechanics," *Physical Review Letters*, vol. 98, no. 2, p. 26102, 2007.
- [4] M. Tan, J. Friend, and L. Yeo, "Direct visualization of surface acoustic waves along substrates using smoke particles," *Applied Physics Letters*, vol. 91, p. 224101, 2007.
- [5] T. Reeder, E. Westbrook, and D. Winslow, "Visualisation of surface acoustic waves," *Electronics Letters*, vol. 6, p. 30, 1970.
- [6] A. Kolomenskii and A. Maznev, "Propagation of laser-generated surface acoustic waves visualized by shake-off of fine particles," *Journal of Applied Physics*, vol. 77, p. 6052, 1995.
- [7] H. Antil, A. Gantner, R. Hoppe, D. Köster, K. Siebert, and A. Wixforth, *Modeling and Simulation of Piezoelectrically Agitated Acoustic Streaming on Microfluidic Biochips*. Springer Berlin Heidelberg, 2008, vol. 60, lecture Notes in Computational Science and Engineering: Domain Decomposition Methods in Science and Engineering XVII.
- [8] T. Leighton, "What is ultrasound?" *Progress in Biophysics and Molecular Biology*, vol. 93, pp. 3–83, 2007.
- [9] S. Fang, S. Zhang, and Z. Lu, "SAW focusing by circular-arc interdigital transducers on YZ-LiNbO₃," *IEEE Transactions on Ultrasonics, Ferroelectrics and Frequency Control*, vol. 36, no. 2, pp. 178–184, 1989.
- [10] T. Wu, H. Tang, Y. Chen, and P. Liu, "Analysis and design of focused interdigital transducers," *IEEE Transactions on Ultrasonics, Ferroelectrics and Frequency Control*, vol. 52, no. 8, pp. 1384–1392, 2005.
- [11] Z. Wang, T. Tang, S. Chen, and B. Chen, "Field analysis and calculation of interdigital transducers with arbitrary finger shapes," *Journal of Physics D: Applied Physics*, vol. 39, pp. 4902–4908, 2006.
- [12] M. Tan, J. Friend, and L. Yeo, "Microparticle collection and concentration via a miniature surface acoustic wave device," *Lap on a Chip*, vol. 7, pp. 618–625, 2007.
- [13] R. Robinson and C. Yu, "Coagulation of Cigarette Smoke Particles," *Journal of Aerosol Science*, vol. 30, no. 4, pp. 533–548, 1999.
- [14] B. Auld, *Acoustic Fields and Waves in Solids*. Wiley, 1973.
- [15] K. Wong and W. Tam, "Analysis of the frequency response of SAW filters using finite-difference time-domain method," *IEEE Transactions on Microwave Theory and Techniques*, vol. 53, pp. 3364–3370, 2005.
- [16] F. Chagla and P. Smith, "Finite difference time domain methods for piezoelectric crystals," *IEEE Transactions on Ultrasonics, Ferroelectrics, and Frequency Control*, vol. 53, pp. 1895–1901, 2006.
- [17] P. Morse and K. Ingard, *Theoretical Acoustics*. MacGraw-Hill, 1968.
- [18] W. L. Nyborg, *Acoustic Streaming*. Academic Press, 1965, vol. 2B, ch. 11, pp. 265–329, eds.: Mason, W. P. and Thurston, R. N.
- [19] C. Bradley, "Acoustic streaming field structure: The influence of the radiator," *Journal of the Acoustical Society of America*, vol. 100, no. 3, pp. 1399–1408, 1996.
- [20] A. A. Doinikov, "Theory of acoustic radiation pressure for actual fluids," *Physical Review E*, vol. 54, pp. 6297–6303, 1996.
- [21] N. Riley, "Steady streaming," *Annual Review of Fluid Mechanics*, vol. 33, pp. 43–65, 2001.
- [22] R. Bowling, "An analysis of particle adhesion on semiconductro surfaces," *Journal of Electrochemical Science: Solid-State Science and Technology*, vol. 132, pp. 2208–2214, 1985.
- [23] Q. Qi and G. Brereton, "Mechanisms of removal of micron-sized particles by high-frequency ultrasonic waves," *IEEE Transactions on Ultrasonics, Ferroelectrics and Frequency Control*, vol. 42, no. 4, pp. 619–629, 1995.